UNIVERSIDAD TÉCNICA FEDERICO SANTA MARÍA

DEPARTAMENTO DE FíSICA

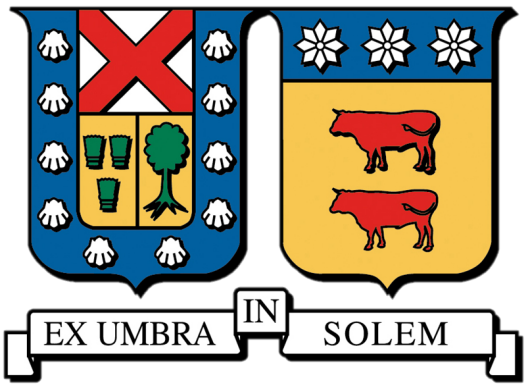

Estimation and Correction of Optical Aberrations induced by Atmospheric Turbulence through Adaptive Optics Systems for Telescopes Using Shack–Hartmann Wavefront Sensors

JOSEFA AGUSTINA ORTIZ URRA

THESIS TO OBTAIN THE DEGREE OF BACHELOR IN ASTROPHYSICS

Guía: Jorge Tapia
Co-referentes: Camilo Weinberger

March-2026

CONSTANCIA DE VALIDACIÓN Y CONFIDENCIALIDAD DE MONOGRAFÍA A REPOSITORIO ACADÉMICO

1.- IDENTIFICACIÓN DEL TRABAJO ACADÉMICO

Tipo de monografía (marcar una opción): ☒ Memoria o trabajo de título ☐ Tesis de Postgrado

Título del trabajo: Estimation and Correction of Optical Aberrations induced by Atmospheric Turbulence through Adaptive Optics Systems for Telescopes using Shack–Hartmann Wavefront Sensors.

Nombre del candidato(a): Josefa Agustina Ortiz Urra

Carrera / Grado: Licenciatura en Astrofísica

Campus: Casa Central Valparaiso **Departamento:** Departamento de Física

2.- VALIDACIÓN DEL PROFESOR GUÍA/DIRECTOR DE TESIS

Yo, Jorge Eduardo Tapia Farías, en mi calidad de profesor(a) guía/director(a) del trabajo académico mencionado anteriormente **DEJO CONSTANCIA** que:

- He revisado esta versión del documento y corresponde a la versión final aprobada del trabajo.
- El trabajo cumple con los requisitos académicos y de formato establecidos por la institución.

3.- EVALUACIÓN DE CONFIDENCIALIDAD POR PROPIEDAD INDUSTRIAL (marcar una opción)

☒ El trabajo **NO contiene** información que amerite confidencialidad y puede ser publicado de inmediato en repositorio con acceso abierto.

☐ El trabajo **CONTIENE** información con potenciales implicancias de propiedad industrial o intelectual y requiere un periodo de confidencialidad (**embargo**) por **(marcar una opción)**:

☐ 6 meses ☐ 12 meses ☐ 2 años ☐ 3 años ☐ 5 años ☐ 10 años

Fundamentación de la necesidad de confidencialidad (obligatorio si se solicita embargo):

4.- FIRMAS

Profesor(a) guía o director(a) de memoria o tesis:

Fecha: 14/05/2026 **Firma:** 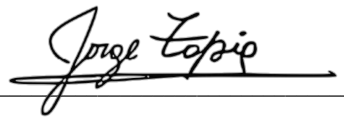

Estudiante o Candidato(a):

Fecha: 14/05/2026 **Firma:** 

Este formulario debe ser insertado como página 2 de la memoria o tesis, completado y firmado por estudiante y profesor(a) antes de la entrega en portal PRISMA de Biblioteca USM.

Abstract

Atmospheric turbulence introduces random fluctuations in the refractive index of the air, which distort optical wavefronts and degrade the image quality of astronomical observations. Adaptive optics (AO) systems are designed to estimate and correct these aberrations close to real time, allowing telescopes to operate close to its theoretical diffraction limit. In this work, the estimation and correction of optical aberrations induced by atmospheric turbulence are studied through computational simulations of an AO system based on a Shack–Hartmann wavefront sensor.

The physical and statistical description of atmospheric turbulence is modeled using Kolmogorov theory with Von Kármán generalization and its effect on wavefront propagation is analyzed through the Fried parameter r_0. Simulations are performed using the Object Oriented Python Adaptive Optics (OOPAO) tool, with system parameters inspired by the PAPYRUS optical bench at the Observatoire de Haute-Provence, France. Wavefront reconstruction is carried out using a modal representation based on Zernike polynomials and correction is applied through a deformable mirror operating in both open-loop and closed-loop configurations.

The performance of the AO system is evaluated for different turbulence strengths using the root-mean-square wavefront error, the Strehl ratio and the resulting point spread function (PSF). The results show that closing the control loop significantly reduces the wavefront error and improves image quality under moderate and weak turbulence conditions. However, under very strong turbulence, the correction becomes limited, indicating the limits of the chosen system configuration. This study highlights the capabilities and limitations of Shack–Hartmann wavefront sensor-based AO systems under controlled and idealized conditions. This work provides a basis for improving future adaptive optics simulations aimed at enhancing astronomical image quality while leaving open the possibility of extending the analysis to more advanced wavefront sensors in order to achieve more robust and realistic system performance.

Acknowledgement

This work has been possible thanks to the support of many people who accompanied me throughout my university life, to whom I owe my deepest gratitude.

First, my sincere thanks go to my supervisor, Professor Jorge Tapia, for giving me the opportunity to work on and learn about a field of study that was completely new to me. I am deeply grateful for his guidance, patience and for encouraging my curiosity in adaptive optics.

My gratitude also extends to Camilo Weinberger, who, despite the time difference between our countries, was always willing to help and share both his knowledge and his passion for optics.

Thanks to my family, who continually supported me in following my dreams and gave me the confidence to ask questions, seek answers and continue questioning the world around me. To my father that deserves a special recognition for revisiting the physics he once learned in order to help me understand the exercises when frustration set in. To my mother, for her unconditional understanding and support, even when she did not fully understand what I was explaining. To my sister, who never fails to make me smile, even in the most chaotic moments.

Special appreciation goes to my beloved Otters USM swimming team, which enriched my university life with invaluable experiences and lifelong friendships. To my classmates and friends, who were always there to support one another through the long and exhausting hours of study in the E400. To all the friends I met during this years, that made this period of my life truly unforgettable, from the very first day playing volleyball to the final goodbye, marked by the traditional jump into the pool. A special grateful to Gonzalo, that was there to believed in me, even when I was not able to do it.

Finally, my gratitude goes to my professors, who constantly motivated us to learn beyond what was required for exams, to find passion in what we studied and to persevere even in moments of exhaustion.

Contents

Chapter 1

Introduction

Atmospheres are a dynamic fluid with continuous variations in chemical composition, temperature, pressure and density throughout its vertical structure. These conditions induce fluctuations in the refractive index, which, when light propagates as a wavefront through the atmosphere, alter its optical path and phase. As a result, astronomical observations are degraded, and the images of observed objects appear blurred, spread and affected by scintillation. To mitigate these effects, Adaptive Optics was developed and has evolved over time to achieve high-resolution astronomical observations. Computational simulations of Adaptive Optics (AO) system are utilized to study different configurations before applying this to real life AO systems.

1.1 Atmospheric turbulence

The atmospheres are an envelope of gasses and particles surrounding celestial bodies, e.g. stars, planets, asteroids. This amount of materials remains around the astronomical object during the rotation around its axis [1]. For the specific case of the Earth atmosphere, the main components are nitrogen (N_2) and oxygen (O_2). It has a vertical structure, meaning that the chemical composition and temperature change vertically.

For the composition case, literature consider a lower and upper layer, called Homosphere and Heterosphere, divided by a thin layer called Turbopause. Pressure and density increase closer to the surface, what allows convection and turbulence at the Homosphere. Due turbulent mixing, the gas composition remains constant, whereas at Heterosphere gas composition become stratified [1].

For the case of the temperature, literature defines the atmospheric layers as the troposphere, stratosphere, mesosphere, and thermosphere, listed from the lowest to the highest. Incoming solar radiation warms Earth's surface, which radiates heat into the troposphere (gradually cooling with altitude), generating turbulent vertical motions. In stratosphere, the presence of ozone causes temperatures to rise again and this is Mesosphere only source of head, leading to a decrease in

temperature once again. Finally, in thermosphere, temperature increase one more, because this layer contains particles able to absorb high-energy solar radiation.

The gas composing the atmosphere is a fluid which can be characterized by a density ρ and a molecular transport coefficient such as the viscosity μ [2]. There are two types of fluid flow: laminar flow is smooth and steady, and turbulent flow is unstable and random. The transition between these two flows is defined by a dimensionless quantity called the Reynolds number (R_e) [3], which involve a numerical relationship between viscous and inertial forces. Low R_e signifies dominance of viscous forces that lead to constant flow and high R_e signifies that inertial forces dominate [4].

Temperature changes give rise to small variations in the atmospheric density, and hence, to the index of refraction (n) [5]. Temperature T and density ρ are related by the ideal-gas equation, $\rho \propto (1/T)$, which is also ties to n [6]. Because temperature differs with altitude, especially when the lower layer have a greater temperature than the upper layer, buoyant convection develops and produces local vortices, commonly called eddies in optical propagation. Within an eddy, there are weak temperature gradients and therefore small gradients of n. Eddies are transported by the wind, and when the wind velocity is high the atmosphere becomes more chaotic, increasing the rate at which n changes. This convective activity and eddy generation characterize Homosphere turbulent flow governed by Navier-Stokes equations, which are generally difficult to resolve. Therefore, atmospheric turbulence is described using statistical models; no theoretical model is accurate for the many cases of turbulence.

For the purposes of this investigation, we studied atmospherics turbulence with Kolmogorov statistical model [7, 8, 9]. The central principles of Kolmogorov's formulation of atmospheric turbulence is the energy cascade theory, a cascade of random turbulent eddies, with various scale sizes, from the outer scale L_0 (on the order of 10–100 m) down to the inner scale l_0 (typically 0.1–10 mm). Energy is injected into the fluid by external sources, such as solar heating, generating large-scale eddies that progressively break down into smaller-scale structures. This cascade continues until the inner scale is reached, where viscous dissipation dominates and the flow becomes laminar [3, 4].

To describe the turbulence, Kolmogorov define the mean square velocity difference between two points in space separated by a displacement vector $\mathbf{r}$, given by a structure tensor. This is not a simple equation, however, if three assumptions about the atmosphere are made, the structure tensor can be simplified. We assumed atmosphere locally homogeneous, locally isotropic and incompressible [2], in order to define the refractive index structure constant (C_n^2), which quantifies the strength of turbulence in units of $m^{-2/3}$ [5] and is considered the key parameter governing turbulence-induced optical path distortions. C_n^2 varies with seasons as well as daily and hourly, geographic location and altitude. Since there is no theoretical model to obtain C_n^2, Hufnagel [5, 10] suggested a way based on experimental observations, such that C_n^2 depends on the wind correlating

factor, the height about the mean see level and the height above the surface of the size.

While C_n^2 characterizes the overall strength of turbulence, AO analyses often require a spectral representation of the refractive-index fluctuations to describe the spatial content of the induced phase aberrations. This information is contained in the power spectral density $\Phi_n(\kappa)$, with κ the angular spatial frequency (spatial wavenumber). $\Phi_n(\kappa)$ follows a $\kappa^{-11/3}$ power law within the Kolmogorov spectrum [4, 5]. In this work, we adopt the Von Kármán spectrum, which extends the Kolmogorov spectrum by incorporating L_0 and l_0, and is therefore more appropriate for our AO system study.

Having established a statistical description of turbulence through C_n^2 and its spectral representation $\Phi_n(\kappa)$, we now introduce a single parameter widely used in AO to quantify the the cumulative effect of turbulence on wave propagation. The Fried parameter, or coherence length, r_0 is defined as the characteristic diameter over which atmospheric turbulence preserves wavefront coherence (the wavefront remains approximately planar) [4]. It is measured in units of length (meters in this work) and expressed as:

$$r_0 = \left(0.423k^2 sec(\beta) \int_0^L C_n^2(z)dz\right)^{-3/5} \tag{1.1}$$

where $k = 2\pi/\lambda$ is the optical wavenumber, L is the propagation path length and β is the zenith angle. r_0 is inversely related to the turbulence strength C_n^2.

To better understand, consider the telescope aperture illuminated by a distorted incoming wavefront. The aperture can be viewed as being divided into coherent patches of typical size r_0. Within each patch, the wavefront remains largely coherent, whereas strong wavefront distortions arise between different patches. Formally, r_0 is defined such that the root-mean-square (RMS) wavefront error induced by atmospheric turbulence over a circular region of diameter r_0 is approximately 1 rad [4], which marks the transition from a largely coherent to a strongly turbulence-degraded wavefront.

To clarify, the physical size of an eddy is not the same as the coherence length r_0. An eddy is a physical turbulent structure, whereas r_0 is a statistical measure resulting from the combined effect of many eddies over a range of spatial scales. This means that a single coherent patch of size r_0 generally contains contributions from many different eddies. Although eddies and r_0 are related, since eddies determine the spatial fluctuations of n, they are not equivalent quantities.

Turbulence also has a temporal statistic [5], the coherence time τ_0, defined as the characteristic time over which the wavefront remains correlated as the turbulence is transported by the wind. Operationally, it is the time it takes the wind to carry a coherent patch by roughly one r_0 across the pupil. A convenient approximation is:

$$\tau_0 \approx 0.53 \left(\frac{r_0}{v_w}\right) \tag{1.2}$$

where v_w is the wind speed. Rather than a time constant, Greenwood [5] describe the same dynamics via the Greenwood frequency f_G,

$$f_G = \frac{1}{2\pi\,\tau_0} \approx 0.43\,\frac{v_w}{r_0} \tag{1.3}$$

Under a finite v_w, the widely used "frozen flow hypothesis" assumes that the v_w carrying the turbulent eddies is much greater than the internal velocity of the eddies, which allows the turbulent layer to act like a "frozen" phase patch sliding across the aperture. Stronger turbulence implies smaller r_0, typically a smaller τ_0 (due to faster fluctuations of coherent patches across the pupil) and larger f_G. Conversely, weaker turbulence yields larger r_0, larger τ_0 and smaller f_G.

When r_0 is small, the aperture is fragmented into many patches and the AO system must correct stronger wavefront distortions, mainly composed of small-scale structures associated with high spatial-frequency variations of n. Conversely, when r_0 is large, the wavefront remains coherent over a larger fraction of the aperture and the distortions, dominated by large-scale structures, are smoother and easier to correct, as they are associated with low spatial-frequency variations of n.

The Fried parameter is also directly related to D. If $D < r_0$, the system can operate close to the diffraction limit, whereas for $D > r_0$ the image quality becomes turbulence-limited and AO is required to compensate for atmospheric distortions [4].

1.2 Source of Light

Light from an astronomical object, such as a star, can be approximated as radiation from a point source. In free space, the light expands as spherical wavefronts (WF). A WF is the surface that joins all points where the wave has the same advance at a given instant. When the wave travels a medium ($n > 1$), where n vary perpendicular to the wave propagation direction, the points forming the wave have a different advance at time, because they traveled at different speeds. This accumulated advanced is called optical path length (OPL) and depends on n fluctuation along the path lenght. Therefore, a WF that propagates in a medium with constants n can be defined as a surface of constant OPL, equivalently to equal propagation delay and constant phase. In a geometrical definition, the rays filling a solid angle of the sphere generated by the propagation of the spherical WF, are locally perpendicular to WF surface [11].

Light is an electromagnetic wave whose electric and magnetic fields oscillate in time and space. A convenient way to describe the propagating field is as a real oscillation whose amplitude and timing vary across space:

$$U(\mathbf{r}, t) = U_0(\mathbf{r})\, sin(\phi(\mathbf{r}) - \omega t), \tag{1.4}$$

where $U_0(\mathbf{r})$ is the amplitude, $\phi(\mathbf{r})$ is the phase, that referred to some point in this cycle[11], and ω

is the angular frequency, which is not disturbed by the atmosphere, therefore the temporal factor remains constant during propagation. In imaging systems the temporal factor is ignored, so the analysis focuses on the spatial variations encoded in $U_0(\mathbf{r})$ and $\phi(\mathbf{r})$.

Since the astronomical object is far away from our telescope, it can be considered to be located at infinity. Therefore, when the propagated WF, which leaves the point source with the same initial ϕ, reaches the telescope aperture, the WF is flat and serves as the reference WF. However, what we observe, and the motivation for this investigation, are the phase differences $\Delta\phi$ that arise either between different points along a given ray path or between distinct rays [11]. As we mentioned previously, atmospheric turbulence causes n variations, which change the OPD of the original WF and consequently its ϕ. This new WF, projected onto the aperture, is called aberrated WF and contains both spatially varying amplitude and phase, however, we are only able to directly detect the amplitude. The only observable quantity of light is the intensity, $I = |U_0(\mathbf{r})|^2$, and from this information the AO system must reconstruct the original phase and correct the aberrated WF.

An important definition is the optical path difference (OPD), also denoted as W, which is the difference between two OPLs, in this case the difference between the reference WF and the aberrated WF. It can express as:

$$\Delta\phi = (2\pi/\lambda)\ \text{OPD} = k\ \text{OPD} \tag{1.5}$$

Measuring the OPD requires wavefront sensors (WFSs), whose different types and operating principles are presented in the next section.

Scientists such as Kirchhoff and Fraunhofer studied wave propagation in detail and arrived at many simplifications by considering the point source to be at infinity. They were able to express $U(\mathbf{r})$ in terms of spatial frequencies and to normalize it over a circular aperture expressed in polar coordinates. The aperture acts as a spatial filter, since it transmits only the portion of the field within its finite diameter, a phenomenon known as diffraction. Therefore, the field projected onto the aperture gives rise to the diffraction pattern, or point spread function (PSF) [5] in the focal plane, which determines the resolution of the system. A larger aperture preserves a broader range of spatial frequencies and therefore yields a narrower, more point-like PSF. Conversely, a smaller aperture suppresses high-frequency components and produces a more spread PSF, resulting in reduced image resolution. Since real telescopes necessarily have finite apertures, the PSF is always diffraction-limited. From now on, we refer to the original PSF at the aperture as the diffraction-limited PSF, which will never be an infinitely small point of light. In fact, the structure of the diffraction-limited PSF consists of a bright central core and a wider background halo [5].

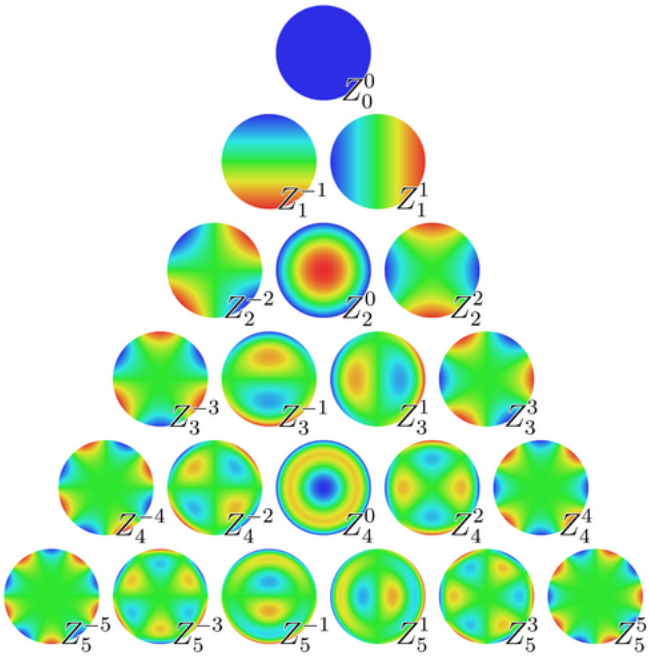

Figure 1.1: Illustration of the first Zernike modes. Among the most commonly cited in the literature are tip Z_1^{-1} (displacement in the x-direction), tilt Z_1^1 (displacement in the y-direction), defocus Z_2^0, astigmatism Z_2^2 and coma Z_3^1. The Zernike mode table by Noll [12] provides the explicit form of these modes, as well as many others, together with a standard single-index ordering.

The diffraction pattern, can be interpreted as the result of superimposed optical aberrations present in WF, which are directly related to the OPD and therefore to $\Delta\phi$. One common way to describe optical aberrations, is to express OPD as a power series in polar coordinates over a circular pupil. Zernike [5, 12] represented the OPD as a linear combination of orthogonal polynomials defined over the unit disk. In this representation, each aberration type corresponds to a Zernike mode, Z_j^i, whose structure is determined by an angular index i and a radial index j. The first Zernike modes are shown in Figure 1.1. The relation between OPD and Zernike modes is given by:

$$W(\rho,\theta) = \sum_{n=0}^{\infty} a_n Z_n(\rho,\theta) \tag{1.6}$$

where a_n are the Zernike coefficients (or Zernike amplitudes), which quantify the contribution of each aberration component [13]. Here, for simplicity, Z_n denotes a single-index ordering of the two-index polynomials Z_j^i, where the index n uniquely maps each pair (i,j) to a specific Zernike polynomial (i.e. to a particular Zernike mode), according to the conventional indexing introduced by Noll [12].

1.3 WFS

A wavefront sensor (WFS) is an instrument used to measure the OPD, or in combination with a deformable mirrors to perform WF correction [11]. As mentioned previously, the human eye can only detect light intensity, and optical detectors are not an exception. From the intensity arriving at the WFS, the phase must be reconstructed using optical designs or interferometric techniques [5].

Interferometric WFSs recover phase information by generating measurable interference patterns. In general, interference arises from the coherent superposition of optical fields and results in a diffraction pattern whose structure encodes information about optical aberrations in the WF. These aberrations are directly related to the OPD and, consequently to $\Delta\phi$ [11, 5].

Non-interferometric optical WFSs, such as the Shack-Hartmann WFS (SH-WFS), use intensity measurements indirectly to estimate local WF gradients, that can be obtain from the displacement of focal spots with respect to their ideal reference positions, or from intensity differences. The local slopes are commonly expressed as dW/dx and dW/dy, meaning that it measures the changes in the two dimensions of the detector. How these local slope measurements are combined to reconstruct the full WF depends on the chosen WF reconstruction method, which is introduced later in this chapter.

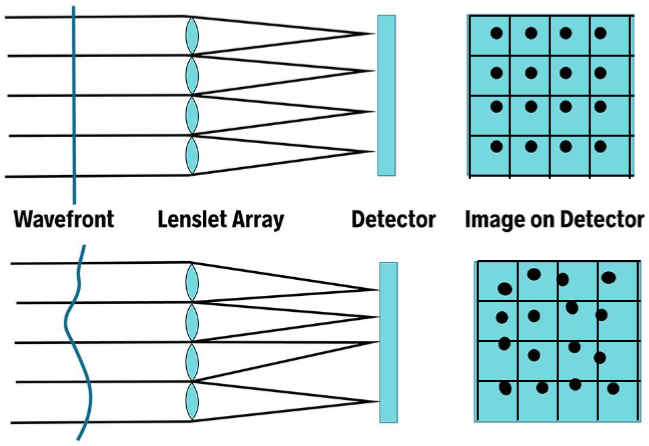

Figure 1.2: SH-WFS composed of a lenslet array with circular sub-apertures and corresponding detectors. The upper diagram shows the SH-WFS receiving a planar WF, while the lower diagram shows the response to an aberrated WF.

For this work, we employed the SH-WFS, one of the most widely used WFSs due to several advantages, including a wide dynamic range, high optical efficiency, white-light capability, the absence of 2π phase ambiguity, the ability to use continuous or pulsed sources and detection of phase singularities [5]. Originally, this sensor was developed to test telescope lens quality, a procedure

known as the Hartmann test.

To illustrate the operating principle of the SH-WFS, the optical configuration shown in Figure 1.2 is considered. The incoming WF passes through a lenslet array, where all lenslets share identical optical characteristics. Each lenslet acts as a subaperture and focuses the incident light onto the detector, producing a localized intensity distribution, commonly referred to as a spot. After proper calibration, the displacement of each spot from its reference position provides a direct measure of the local WF slopes (dW/dx and dW/dy) [5]. In addition, the lenslet array spatially segments the PSF and prevents light leakage between neighboring subapertures. Such leakage corresponds to spot spillover into adjacent detector regions, which would otherwise contaminate the measurements and bias the estimated slopes. This segmentation preserves the integrity of the position signal associated with each pupil location [11].

Geary [11] relates the local WF slopes to the displacement of each focal spot through the transverse ray aberration T, defined as the distance between the actual spot position and the reference spot position in the detector plane. If T is known, together with the pupil radius r, the radius of curvature of the reference sphere R, and the refractive index n of the medium within the sensing optics (typically air and treated as constant), the local WF slopes can be expressed as

$$\left(\frac{dW}{dx}, \frac{dW}{dy}\right) = \frac{-nr}{R}\left(T_x, T_y\right) \tag{1.7}$$

To compute T_x and T_y, the reference spot position, commonly called centroid, must first be estimated. The centroid coordinates (x_i^0, y_i^0), where i indexes the detector (or subaperture), are calculated as an intensity-weighted average of the pixel coordinates over the detector area, that is, each pixel contributes proportionally to the intensity measured at that pixel. If the coordinates of the actual spot position are (x_i, y_i), the transverse aberration components are then obtained as $(T_x, T_y) = (x_i, y_i) - (x_i^0, y_i^0)$. In the absence of aberrations, the actual spot position coincides with the centroid, thereby $T = 0$ and the local WF slopes are zero.

The slopes measured by the WFS are used to reconstruct the wavefront phase. Several reconstruction approaches are summarized in Figure 1.3. For the purposes of this work, we focus on a modal phase representation combined with zonal commands for correction.

When the WF is expressed in terms of coefficients of the modes of a polynomial expansion over the entire pupil (i.e, Zernike modes and their corresponding coefficients), it is said to be modal [5]. From Eq. 1.6, it follows that the OPD and therefore the phase, can be obtained once the coefficients a_n are known. These coefficients can be estimated from the measured slopes and the interaction matrix $\mathbf{B}$.

The interaction matrix is constructed by applying a set of Zernike modes with known amplitudes to the DM and recording the corresponding slopes measured by the SH-WFS. The matrix is built

column by column, with each column associated with a single Zernike mode. Its rows contain the measured slopes for all subapertures, arranged as x-slopes followed by y-slopes. This entire procedure constitutes the calibration of the AO system.

To describe the correction process, it is also necessary to understand the structure of an AO system. This is addressed in the next section.

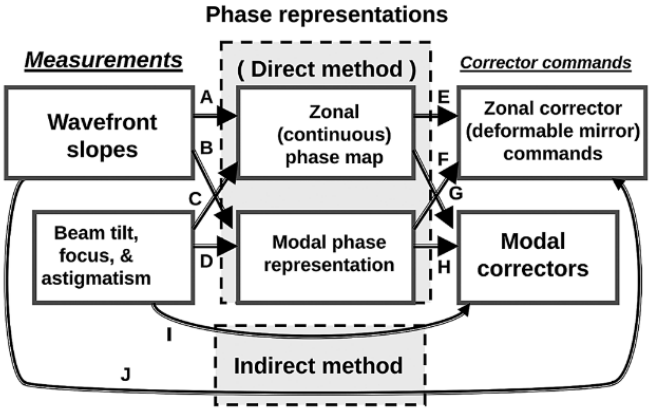

Figure 1.3: Various paths of WF representation and corrector commands. Illustration from [5]

1.4 Adaptive optics systems

We have already studied how atmospheric turbulence modifies the OPL of light and generates an aberrated WF. WFSs and the phase-correction methods belong to the scientific and engineering discipline known as adaptive optics. AO is a technique which eliminates aberrations from optical systems by using at least one deformable mirror which alters its shape to account for the aberrations [14]. This technology has been used in astronomical observations, retinal imaging, laser beam shaping and other fields [15]. In astronomy in particular, the desire to propagate an undistorted beam of light or to receive an undistorted image, has made the field of AO discipline in its own right [5]. AO has become essential for optical systems affected by dynamic aberrations such as those produced by atmospheric turbulence. The main challenge arises from the fact that turbulence changes continuously, producing n fluctuations, and therefore, changes in the optical properties of the WF reaching the telescope. This is the central difficulty of AO: the system can never correct aberrations perfectly in real time. Nevertheless, continuous technological advances, especially in sensor speed, computational power and deformable mirror response, steadily improve the achievable correction speed and overall system performance.

The Nyquist-Shannon sampling theorem states that the sampling frequency f_s is at least twice the highest significant frequency in the signal [5], i.e. $f_s > 2\, f_G$, in order to accurately reconstruct

a continuous time signal, or equivalently, to recover the correct phase information in an AO system. In practical applications, several AO manufacturers, such as ALPAO [16], deploy deformable mirrors capable of operating at sampling frequencies in the range of 500 Hz to 2 kHz, consistent with typical atmospheric Greenwood frequencies $f_G \approx 200\,\text{Hz}$ encountered in astronomical systems.

AO is inspired by the active focusing mechanism of the eye–brain system. The brain interprets an image, determines the correction and applies that correction through bio-mechanical movement of parts of the eye, such as the lens or cornea [5]. This natural AO process operates in a closed loop.

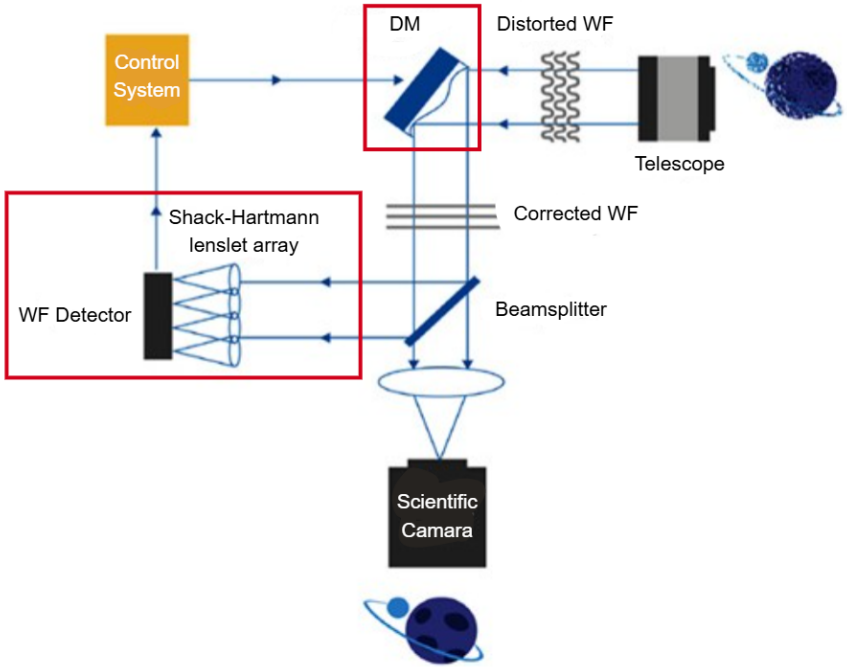

Figure 1.4: Image formation in an AO system with close-loop configuration. Elements inside the red squares correspond to the SH-WFS.

The overall process is illustrated in Figure 1.4. Light enters the telescope through the aperture, pupil and secondary mirrors, and then propagates through the optical bench, where the AO system is located. This system is composed of three major elements: deformable mirror (DM), WFS and control system. The DM is a continuous reflective surface whose mechanical structure includes actuators that deform the mirror to compensate aberrations. The control system receives the measurements from the WFS and converts them into correction commands sent to the DM.

For a DM with zonal corrector, a mode-to-command matrix $\mathbf{M}$ is required to translate the measured Zernike coefficients into actuator commands. These actuator commands (also referred to as DM coefficients) specify how much each actuator should move, typically through electrical drive signals, and therefore determine the actuator stroke. When an actuator is driven, it deforms the

mirror surface over a finite region. The resulting surface deformation produced by a unit push/pull is called the influence function (IF). The DM surface is then modeled as a linear superposition of all influence functions weighted by the actuator commands, allowing the mirror to approximate the desired corrective shape that compensates the OPD of the aberrated wavefront. A key practical limitation is actuator coupling: because the mirror surface is continuous, the deformation induced by one actuator overlaps with that of neighboring actuators, so the IF are not perfectly independent.

These corrections must be applied continuously over time, a single correction is not sufficient to achieve good AO performance. At an initial instant, the system corrects the aberrated WF. Once a correction is applied to the DM, the SH-WFS measures the remaining WF error (the residual) and provides updated information for the next correction. These are the ways to operate an AO system, open-loop and close-loop, respectively.

In the open-loop configuration, the WF is measured by the WFS and the estimated correction is then applied to the DM. Open-loop operation can be useful, for example, when determining optical turbulence parameters from open-loop slopes [15]. A key drawback is that it is highly sensitive to calibration errors and does not account for previous DM commands, because the WFS does not measure the residual WF after correction.

In closed-loop operation, analogous to the eye–brain system, the DM is placed before the beamsplitter, as shown in Figure 1.4. In this case, the incoming WF is partially compensated by the DM before being sampled by the WFS. The WFS therefore measures only the residual WF, i.e., the difference between the current incoming aberration and the correction currently applied by the DM. Although the optical aberrations varies continuously, the correction applied to the previous WF remains partially useful for the next incoming WF, even if it is not perfect. This is why the residual error does not decrease monotonically; however, the control loop continuously attempts to drive it toward zero. The closed-loop configuration is particularly powerful because it can compensate, over successive iterations, for certain calibration errors that would otherwise accumulate.

In AO different techniques can be combined to achieve improved performance. Regarding corrector operation, the closed-loop configuration is one of the most widely used approaches, however, its first iteration, when the DM is initially flat, is effectively equivalent to open-loop operation. It is important to note that neither configuration can correct aberrations perfectly in real time due to unavoidable delays, measurement noise, and continuously evolving turbulence.

1.5 AO simulation tools

Simulation is an efficacious way to do AO research. Researchers can analyze performance of AO systems without an actual system and can predict the performance of different algorithms

conveniently [17]. The list of AO simulators in the community has constantly been growing, guided by different needs and purpose [18]. In this investigation we use Object Oriented Python Adaptive Optics (OOPAO), a simulation tool based on Object Oriented Matlab Adaptive Optics (OOMAO) to adapt its philosophy to the Python language. The principle of OOPAO is that the light from a given point source can be propagated through multiple objects (Atmosphere, Telescope, DM, WFS, etc.) among which experimental features can be input.

The specific parameters and configurations employed in the simulations of this study will be detailed in a subsequent chapter.

Chapter 2

Objective and Scopes

The general objective of this work is to understand the modeling of atmospheric turbulence and the estimation and correction of the optical aberrations induced on astronomical wavefronts through AO systems based on Shack–Hartmann WFSs, using computational simulations as the main study approach.

To achieve this, specific objectives were established. First, understand the physical origin of atmospheric turbulence and the Kolmogorov statistical model that describes its spatial structure. Second, study the operational parameters of real AO systems and the typical atmospheric conditions encountered by ground-based telescopes. Third, to comprehend and implement AO simulations using the Python-based tool OOPAO. Finally, simulate an AO system based on a Shack–Hartmann WFS, in both open- and closed-loop modes, under realistic operating conditions of the OHP telescope, and evaluate its wavefront estimation and image quality improvement using quantitative metrics such as RMS wavefront error, Strehl ratio, and PSF.

This work is limited to simulated scenarios and does not include experimental validation or observations of real astronomical targets. Atmospheric turbulence is represented only with the Kolmogorov model, and changes in observing conditions are introduced exclusively through variations of the Fried parameter, while the remaining atmospheric parameters are kept constant. The simulations consider a point source with known phase information, which simplifies the analysis and allows direct visualization of reconstruction modes and residual errors, enabling a controlled comparison between the uncorrected case and the wavefronts estimated and corrected by the AO system. Therefore, the conclusions describe the system behavior under controlled and idealized conditions, rather than under real observing conditions.

Chapter 3

Methodology

As mentioned previously, the simulations presented in this work were carried out using the OOPAO simulation tool. This platform allows the definition and control of the main components of an AO system, including the source characteristics, telescope parameters, atmospheric turbulence, DM geometry, WFS configuration, number of Zernike modes, interaction matrix and the resulting PSF.

The configuration of the elements was chosen to represent a typical SH-WFS, reproducing atmospheric conditions and telescope scale comparable to those at the Observatoire de Haute-Provence (OHP) [19]. We also considered the large aperture of the OHP telescope, which has been operational since June 2022. The optical bench of OHP was specifically designed for research and development in AO as well as for educational purposes. Its primary objective is to test new hardware components, as well as new WF sensing and control strategies, serving as a pathfinder for advanced AO systems foreseen for the next generation of Extremely Large Telescopes (ELTs) [20].

3.1 OHP telescope

The OHP is located in the south of France, at an altitude of 650 meters, and is characterized by challenging observing conditions, with cloudy weather during approximately 20% of the nights [19]. The telescope, named T152, has a total diameter of 1.52 m and a useful aperture of 1.5 m. The original WFS of the optical bench is a Pyramid WFS (PY-WFS). However, in order to compare the performance of the PY-WFS with a SH-WFS, an additional parallel bench equipped with a SH-WFS was implemented. The optical bench is composed of six main subsystems: a telescope simulator unit used for alignment procedures, a calibration unit operating at a wavelength of 635 nm to compute the interaction matrix, a common optical path shared by all channels, a science path including the scientific camera, the PY-WFS branch and the SH-WFS branch.

3.2 Simulation parameters

The first step in the simulation setup is the configuration of the point source, referred to as a Natural Guide Star (NGS) in OOPAO. According to [19], the limiting observable magnitude for the SH-WFS in the visible wavelength range lies between 4 and 5. Based on this constraint, a optical band V was set and a magnitude of 5 was selected.

The telescope was configured with a diameter of 1.5 m, a pupil resolution of 112×112 (112 pixels across the pupil), determined by the number of lenslet per row in the SH-WFS and the resolution of each microlens, and a central obstruction of 0.1, corresponding to 10% of the telescope diameter. The pupil resolution setting is geometrical compatible with 14×14 subapertures of SH-WFS lenslet array and follows the recommendations provided in [18] for a sufficiently well-resolved pupil. The obstruction accounts for the presence of the secondary mirror, which blocks part of the light collected by the primary mirror and provides a more realistic representation of the optical geometry.

The DM was simulated using the Fried geometry (rectangular DM) aligns with the corners of the subapertures [5], i.e. each actuator is located at the corner of 4 subapertures [8]. This distribution of the actuators, ensures that each actuator influences multiple neighboring subapertures, leading to more pronounced slope variations and clearer SH-WFS measurements. Although this configuration introduces spatial leakage between subapertures, is fully accounted for the interaction matrices. For this reason, the Fried geometry remains a standard choice.

For the DM we set 17 actuators across the pupil diameter [19], i.e. the rectangular DM has dimensions 17×17, and a mechanical coupling of 0.45. Formally, the mechanical coupling is defined such that if an actuator is displaced an arbitrary value 1, the resulting deformation at a radial distance equal to the actuator pitch is a fraction of this value. The actuator pitch, defined as the distance between neighboring actuators, is automatically computed as the ratio between the telescope diameter and the number of actuators across the pupil. A higher mechanical coupling value, such as 0.45, corresponds to a softer and more continuous DM surface, leading to increased overlap between actuator IFs. While this results in stronger spatial leakage, it provides a more realistic representation of the physical behavior of continuous DM.

We simulated the SH-WFS with 14×14 subapertures, a light ratio of 0.5 and a threshold of 0.1. The light ratio is the criterion to select the valid subaperture based on flux considerations. The subaperture is consider valid when maximum flux multiply by the light ratio is equal or bigger than the flux of an individual subaperture. In our case the flux of an individual subaperture must be bigger or equal to the 50% of the maximum flux to be valid. The threshold is utilized to validate the pixels inside a detector, which it maximum intensity multiply by the threshold muss be bigger or equal to the pixel intensity. This is important to avoid noise in the centroid calculations. Both criterion, light ratio and threshold, are useful to decrease the noise in the phase reconstruction

process.

The atmosphere was simulated using the Kolmogorov model (with Von Kármán generalizations) with $L_0 = 25\ m$ and two turbulent layers. The first layer is located at 0 m altitude and contributes $C_n^2 \propto 0.7\ m^{-2/3}$, with a wind speed of 5 m/s and a wind direction of 0°. The second layer is located at 1000 m altitude and contributes $C_n^2 \propto 0.3\ m^{-2/3}$, with a wind speed of 10 m/s and a wind direction of 20°. We used four values of r_0, 0.05, 0.08, 0.12 and 0.2 m, to perform open- and close-loop simulations.

The interaction matrix $\mathbf{B}$ is automatically constructed using OOPAO. Its computation requires the specification of the NGS, telescope, atmospheric model, DM, SH-WFS, the modal to command matrix $\mathbf{M}$, actuator stroke and the number of simultaneous WFS measurements. A push–pull stroke of $2 \times 10^{-9}\ m$ was applied, corresponding to the actuator displacement. This small stroke ensures operation within the linear response regime of the WFS. The number of simultaneous WFS measurements was set to 1, meaning that the $\mathbf{B}$ was built column by column, without parallel excitation of multiple modes. Measurement noise was disabled during the calibration process in order to obtain an ideal interaction matrix. We utilized 200 Zernike modes to calibrated B.

3.3 Simulation steps

Since in the simulation we know the OPD without any additional calculations, we can use it to reconstruct the Zernike amplitudes and then use those amplitudes to return to an estimate OPD (i.e., a reconstructed OPD). Although this procedure does not represent an actual AO measurement, it is used here solely to visualize the modal content of the WF and the residual as a function of r_0. This procedure is based on Eq. 1.6. The matrix representation is given by

$$\mathbf{W} = \mathbf{a}\,\mathbf{Z} \tag{3.1}$$

where $\mathbf{W}$ is a vector containing the OPD value at each pixel, $\mathbf{a}$ is the vector of Zernike amplitudes, and $\mathbf{Z}$ is a matrix that specifies the Zernike mode values at each pixel [5]. In what follows, the OPD is expressed in units of length and is referred to as "phase" for simplicity and consistency with common AO terminology, although OPD and optical phase are not strictly the same quantity.

We compute the open-loop performance for the four values of r_0. The NGS is propagated through the telescope pupil, the atmosphere is then applied and the resulting WF is measured with the SH-WFS. Local WF slopes are automatically obtained and organized into a vector $\mathbf{s}$ (all x-slopes followed by all y-slopes). We can estimated $\mathbf{a}$ from

$$\mathbf{s} = \mathbf{B}\,\mathbf{a} \tag{3.2}$$

To obtain $\mathbf{a}$, we apply the pseudo-inverse of $\mathbf{B}$.

After the initial open-loop correction, the closed-loop simulation measures and corrects the residual aberrations. For each value of r_0, we run 300 iterations. At each iteration, the DM coefficients $\mathbf{u}$ are updated by adding an incremental correction to the previous command vector:

$$\mathbf{u}_{\text{new}} = \mathbf{u}_{\text{previous}} - g(\mathbf{M}\,\mathbf{a}) \tag{3.3}$$

where g is a coefficient with values between 0 and 1. We used $g = 0.1$, meaning that at each iteration the DM applies 10% of the newly estimated correction. A small g results in a smoother and slower correction, but with reduced noise. The negative sign is required because the DM must apply the opposite phase to compensate the measured aberration.

The metric standard deviation σ represents the RMS WF error and quantifies the spatial variability of the OPD across the pupil. A small σ is equivalent to a more coherent OPD across the pupil. It can be written as

$$\sigma^2 = \langle(\text{OPD} - \langle\text{OPD}\rangle)^2\rangle \tag{3.4}$$

The metric Strehl ratio (SR) is defined as the ratio between the peak intensity of the corrected PSF and that of the diffraction-limited PSF (PSF0), given by [14] as

$$\text{SR} = \frac{max(\text{PSF})}{max(\text{PSF0})} \tag{3.5}$$

To accurately compute the PSF, a zero-padding factor of 6 was used to ensure adequate sampling of the PSF while keeping the computational cost reasonable.

Chapter 4

Results

This chapter presents the results obtained from the numerical simulations of the AO system described in the previous sections. We analyze how the system behaves in open-loop and closed-loop, and we evaluate its ability to correct an aberrated WF generated under different atmospheric conditions, parameterized by r_0. The results are presented in terms of reconstructed WF, residual errors σ, SR evolution and the final PSF, including normalized PSF profiles.

Before presenting the performance of the AO system, it is relevant to examine how the phase reconstruction using the first 200 Zernike modes behaves and how the residual changes with the value of r_0. Figure 4.1 shows the original phase compared with the reconstructed phase and the residual. The first aspect to notice is that the phase amplitude varies more when r_0 is small. We observe that the modal content in the original and reconstructed phases are similar in shape and color, where the color indicates the phase amplitude in μm. However, the phase variation in the original phasemap is well represented by a colormap, while the reconstructed phase is smooth and continuous across color transitions. We also note that the color distribution of the original phase decreases as r_0 increases. The residual map also shows the color distribution and tends toward zero phase amplitude as r_0 increases.

Starting with the AO system results, the open-loop simulation is shown in Figure 4.2 to examine the behavior of the Zernike amplitudes for different values of r_0 and to evaluate the reconstruction performance of the Zernike coefficients. No phase correction has been applied. It can be observed that, for all four values of r_0, the reconstruction of the Zernike amplitudes is generally accurate for the first 100 Zernike modes. Although 200 Zernike modes were reconstructed, only the first 100 are shown, since higher-order mode amplitudes are close to zero and therefore do not clearly reveal differences between the original and reconstructed phases.

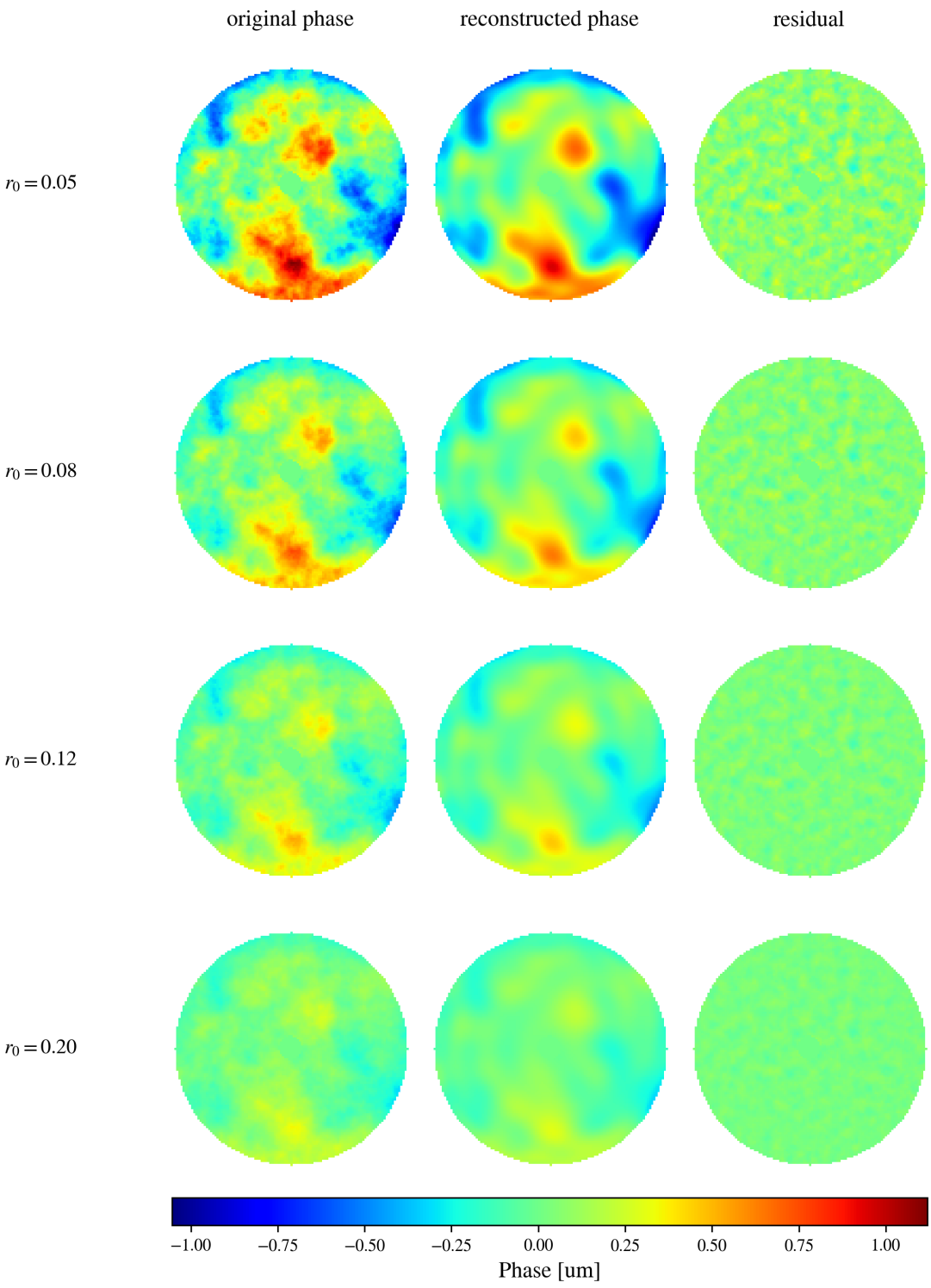

Figure 4.1: The first column shows the values of r_0 in meters. The second, third, and fourth columns display the original OPD map, the reconstructed OPD map using the first 200 Zernike modes, and the corresponding residual, all projected onto the pupil, respectively. The phase amplitude is expressed in μm and show the colorbar.

The overall amplitude of the Zernike coefficients decreases as r_0 increases, in agreement with the results shown in Figure 4.1. Additionally, for each value of r_0, the amplitudes of the first 10 Zernike modes are noticeably larger than those of higher-order modes, and this effect becomes less pronounced as r_0 increases. Finally, although the reconstruction of Zernike amplitudes generally becomes more challenging for higher-order modes, this limitation is not clearly visible in the present results.

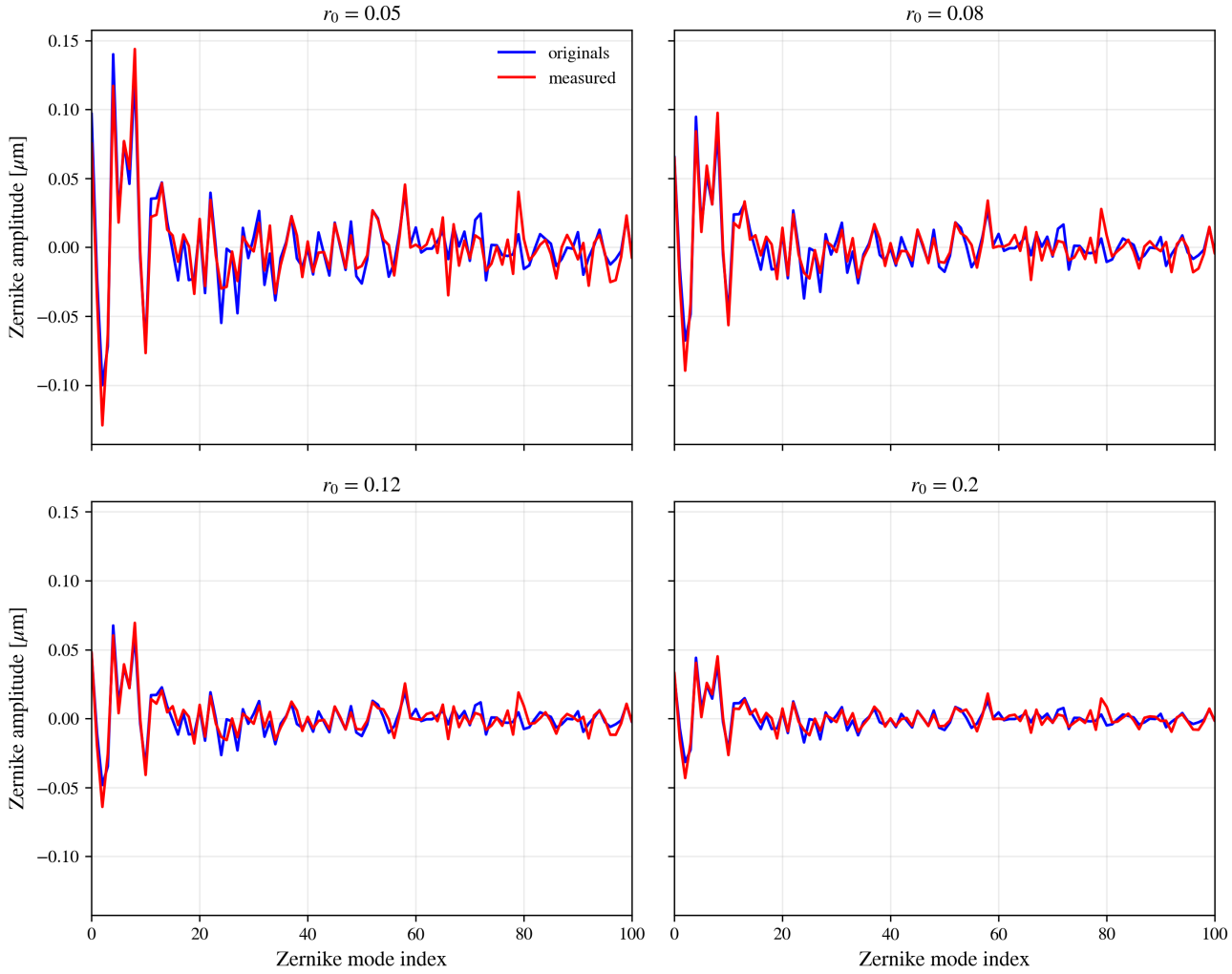

Figure 4.2: The four panels show the Zernike amplitudes (in μm) as a function of the Zernike mode for each value of r_0, indicated at the top of each panel.

We simulated the closed-loop operation over 300 iterations for the previous values of r_0, with the loop being closed after the first 10 iterations. Figure 4.3 shows the temporal evolution of σ. Initially, the curves start at different σ values, with smaller r_0 corresponding to larger initial WF errors. After the loop is closed, σ decreases sharply in all cases. As the iterations progress, the curves converge toward a quasi-stationary value of σ, been the only exception the case with

$r_0 = 0.05\ m$.

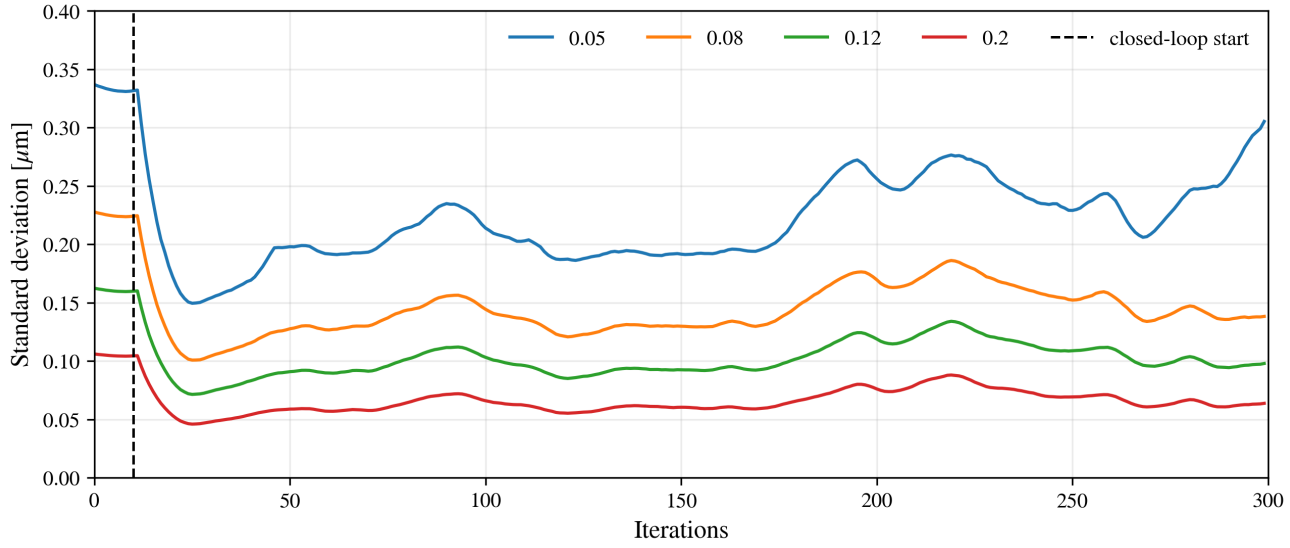

Figure 4.3: Evolution of standard deviation σ (RMS WF error), for four values of the r_0 (in meters). The control loop is closed at iteration 10.

Figure 4.4 shows the temporal evolution of the SR for the r_0 values. The initial SR values differ among the cases and increase with increasing r_0. Once the loop is closed, the SR increases sharply for $r_0 = 0.20$, $r_0 = 0.12$, and $r_0 = 0.08\ m$. In contrast, the case with $r_0 = 0.05\ m$ shows a small increase after loop closure. Furthermore, after closing the loop and the system reaches steady state, the SR remains approximately constant for all cases.

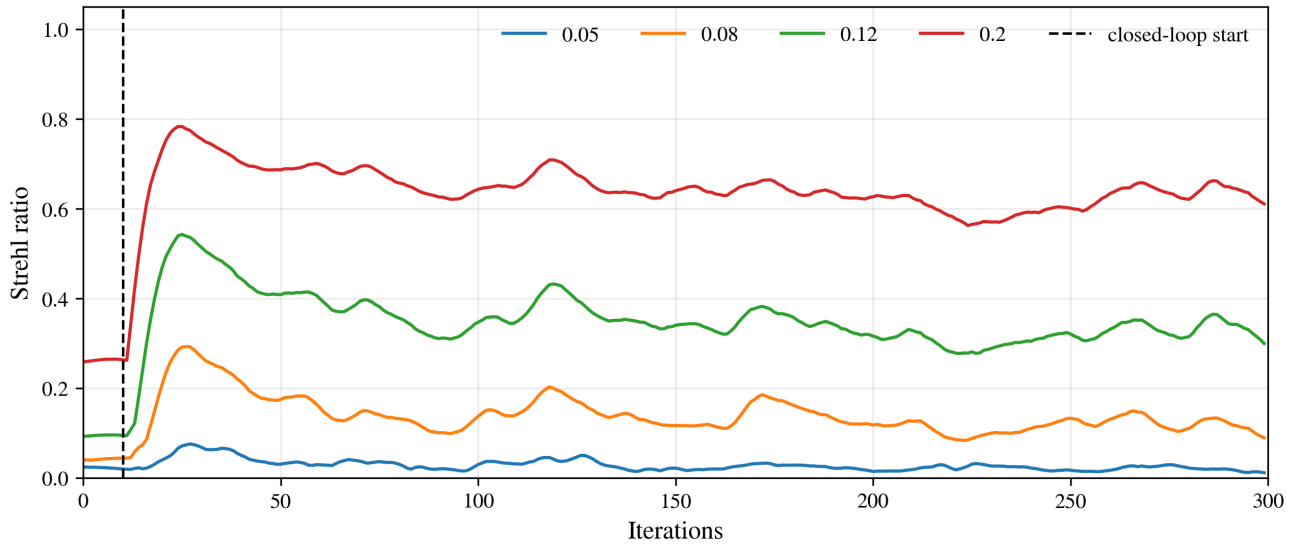

Figure 4.4: Evolution of Strehl Ratio (SR), for four values of the r_0 (in meters). The control loop is closed at iteration 10.

PSF represents the light intensity distribution in the focal plane of the telescope. Figure 4.5 shows the PSF obtained for r_0 values. It can be observed that the peak intensity of the PSF increases as r_0 increases, which is also evident in the corresponding normalized PSF profiles.

For $r_0 = 0.05\ m$, no clear intensity peak is visible and the PSF profile does not exhibit a well-defined central maximum. The case with $r_0 = 0.08\ m$ shows a more structured PSF, although the peak intensity remains relatively low. For $r_0 = 0.12\ m$, a pronounced central intensity maximum becomes clearly visible, surrounded by lower-intensity regions. The best PSF is obtained for $r_0 = 0.20\ m$, however, it still does not fully reach the diffraction-limited PSF. In this case, a bright central core is observed, surrounded by a faint halo, resembling an Airy-like disk structure.

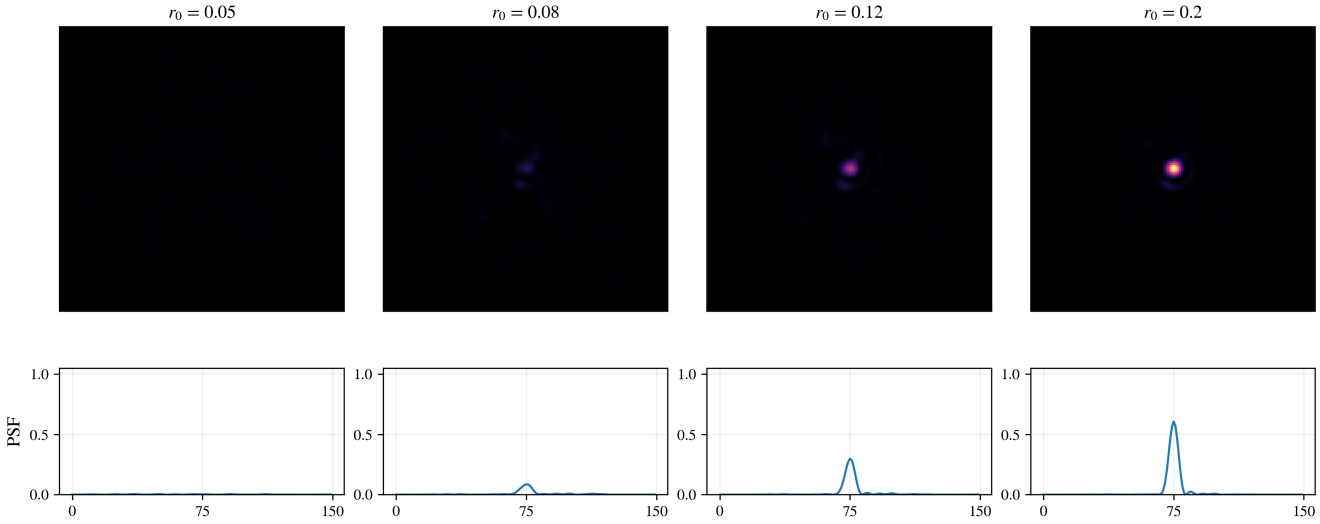

Figure 4.5: The first row shows the PSF obtained after closed-loop correction for each value of r_0. The second row presents the corresponding normalized radial profiles of the final PSF.

Chapter 5

Discussion

As expected from Kolmogorov turbulence, the OPD increases as the turbulence becomes stronger, i.e., for smaller values of r_0. This trend is clearly visible in the original phase maps, where the phase amplitude is noticeably larger under stronger turbulence than in cases with weaker turbulence.

The detailed color distribution observed in the original phase maps arises from the small-scale structure of atmospheric turbulence. As the WF propagates through a medium with n fluctuations, it accumulates phase along the optical path. The spatial appearance of this accumulated phase depends on the spatial frequency of those fluctuations: rapid variations (high spatial frequencies) produce fast phase changes across the pupil, generating small-scale structure, whereas slower variations (low spatial frequencies) lead to smooth large-scale distortions. Consequently, smaller r_0 values are expected to produce phase maps with stronger small-scale structure, while larger r_0 values result in smoother phase distributions.

The small-scale color distribution is mostly missing in the reconstructed phase because the reconstruction uses only a limited number of Zernike modes, which act as a scale filter and allow only the larger spatial scales to pass. Since only global structures across the pupil are retained, the reconstructed phase map appears smooth, while most of the small-scale structure remains in the residual maps, reason why the residual also shows detailed color distribution. The residual becomes less granular as r_0 increases, since the original phase contains fewer small-scale variations, making the reconstruction nearly flat.

The closed-loop simulations show a well-behaved σ for almost all cases, except for $r_0 = 0.05\ m$. As expected after closing the loop, σ decreases because it quantifies the spatial variability of the OPD across the pupil. At each iteration, the DM applies successive corrections that make the OPD distribution smoother across the pupil, reducing the differences between points and therefore lowering σ.

As the iterations progress, an approximately stationary value of σ indicates that the closed-loop has reached a stable operating regime. In practice, σ does not converge to zero because the

correction is limited by temporal effects (finite update rate and delays) and by spatial effects: the system cannot fully correct the smallest-scale WF structures, so a residual error remains.

For the extreme case of $r_0 = 0.05\ m$, the chosen correction configuration is insufficient under such strong turbulence and the system approaches is limited by the number of SH-WFS subapertures. The number of subapertures is inversely related to the spatial sampling period d and d is inversely related to the spatial Nyquist limit f_{Ny} by $f_{Ny} = 1/2d$ [5]; therefore, when the number of subapertures is small, d is large and f_{Ny} is small. All the spatial frequencies above f_{Ny} cannot be detected because they are finer than the minimum spatial scale the WFS can measure; instead those high-spatial frequencies are mistakenly recorded as low-spatial frequencies that do not actually exist. This effect called aliasing appears as undulation and absence of stability in the curve of RMS WF error. Increasing the number of subapertures reduces aliasing but also lowers the signal to noise ratio (SNR), since fewer photons are collected per subaperture. Thus, a trade-off is required between subaperture count and pixels per subaperture.

Nevertheless, closed-loop still achieves a substantial reduction of σ during the first 150 iterations, indicating robust performance even under severe conditions. In practice, atmospheric conditions corresponding to this value of r_0 are generally considered too poor for high-quality astronomical observations.

The SR shows the opposite trend to the metric σ, since SR reflects the improvement of the PSF. In agreement with the literature [14, 15, 21], SR increases shortly after the closed-loop starts and then remains approximately constant, as the PSF becomes less spread and more concentrated around its peak. The exceptional case, the same one identified with the σ metric, shows little to no improvement, maintaining a PSF close to its initial state. In all cases, the PSF does not fully reach the ideal, unperturbed (diffraction-limited) PSF, indicating that the chosen correction configuration is not sufficient to achieve diffraction-limited performance. Nevertheless, the improvement is most significant for the largest value of r_0.

By examining the PSFs, the behavior of SR becomes easier to interpret, since the PSF morphology is directly related to SR: higher SR values correspond to a stronger concentration of light in the central peak. In the exceptional case, the light remains strongly spread across the focal plane due to severe atmospheric turbulence, which explains why SR does not show any noticeable improvement.

It is important to note that the ideal PSF produced by a perfectly planar wavefront is not an infinitely small point. Even in the absence of aberrations, a finite telescope aperture causes diffraction, resulting in an Airy pattern. In addition, real telescope pupils are not perfectly circular and unobstructed. The central obstruction and support structures (spiders) further reduce the capacity of the WFS to estimate the aberrated WF, introducing holes in the slope measurements and permanent aberrations by diffraction by the presence of the spiders. Additionally, for the same reason, a real PSF will never be a perfect point source, even under correction.

Chapter 6

Conclusions and future work

During this work, we achieved the general and specific objectives: we understood the modeling of atmospheric turbulence and implemented the estimation and correction of WF distortions by simulating an AO system based on a SH-WFS. We identified the typical operating parameters of real AO systems at the OHP telescope and used OOPAO computational tool to simulate open- and closed-loop operation of an SH-WFS-based AO system. We studied the limits of a standard SH-WFS-based AO correction under realistic turbulence strengths (r_0=0.05, 0.08, 0.12 and 0.20 m) and evaluated performance using RMS WF error, SR and PSF.

Simulations show that closing the loop reduces RMS WF error and improves image quality (higher SR and a more concentrated PSF), reaching a quasi-stationary regime in most cases. The most severe condition constitutes the main limitation, where correction is not maintained as stable and the SR improvement is minimal, indicating that the chosen correction configuration is insufficient under very strong turbulence.

Future work should focus on improving spatial correction (e.g. higher modal order, more actuators and subapertures), and increasing realism by varying additional atmospheric parameters and adopting a more realistic telescope pupil, including central obstruction, spiders and photon-noise in the WFS.

In summary, this work helped identify the main performance limits and improvement opportunities of SH-WFS base AO system, including an extreme regime used to probe system boundaries. These findings provide guidance for implementing real AO systems, where additional effects not modeled here will also matter, in order to achieve sharper PSFs and higher image resolution, which are essential for resolving fine astrophysical structures and detecting faint companions. Emerging approaches, such as pyramid WFS, calibration and diagnostics assisted by AI, represent natural extensions of this study.

Bibliography

[1] István Lagzi, Róbert Mészáros, Györgyi Gelybó, and Ádám Leelőssy. *Atmospheric Chemistry*. Eötvös Loránd University, Budapest, Hungary, 2013.

[2] G. K. Batchelor. *The Theory of Homogeneous Turbulence*. Cambridge University Press, Cambridge, England, 1st edition, 1953.

[3] Liesebet E. Gravley. *Comparison of Climatological Optical Turbulence Profiles to Standard, Statistical and Numerical Models Using HELEEOS*. Master's thesis, Air Force Institute of Technology, Air University, Department of the Air Force, Wright-Patterson Air Force Base, Ohio, 2019.

[4] Mingjian Cheng and Martin Lavery. Optical angular momentum interaction with turbulent and scattering media. In *Structured Light for Optical Communication*, pages 237–257. Elsevier, Oxford, 2021.

[5] Robert K. Tyson and Benjamin W. Frazier. *Principles of Adaptive Optics*. CRC Press, Taylor & Francis Group, Boca Raton, FL & Abingdon, UK, 5th edition, 2022.

[6] Steven T. Fiorino, Richard J. Bartell, Matthew J. Krizo, Brandon T. McClung, J. Jean Cohen, Robb M. Randall, and Salvatore J. Cusumano. Broad-spectrum optical turbulence assessments from climatological temperature, pressure, humidity, and wind. *Journal of Directed Energy*, 3(3):223–238, 2009.

[7] A. N. Kolmogorov. The local structure of turbulence in incompressible viscous fluid for very large reynolds numbers. *Doklady Akademii Nauk SSSR*, 30:301–305, 1941. English translation available in Proceedings of the Royal Society of London A.

[8] A. N. Kolmogorov. Dissipation of energy in the locally isotropic turbulence. *Doklady Akademii Nauk SSSR*, 32:16–18, 1941. English translation available in Proceedings of the Royal Society of London A.

[9] A. N. Kolmogorov. A refinement of previous hypotheses concerning the local structure of turbulence in a viscous incompressible fluid at high reynolds number. *Journal of Fluid Mechanics*, 13:82–85, 1962.

[10] Larry B. Stotts and Larry C. Andrews. Improving the hufnagel-andrews-phillips refractive index structure parameter model using turbulent intensity. *Optics Express*, 31(9):14265–14278, 2023.

[11] Joseph M. Geary. *Introduction to Wavefront Sensors*, volume TT18 of *Tutorial Texts in Optical Engineering*. SPIE Press, Bellingham, WA, 1995.

[12] Robert J. Noll. Zernike polynomials and atmospheric turbulence. *Journal of the Optical Society of America*, 66(3):207–211, 1976.

[13] Max Born and Emil Wolf. *Principles of Optics: Electromagnetic Theory of Propagation, Interference and Diffraction of Light*, chapter 9. Cambridge University Press, Cambridge, 7th (expanded) edition, 1999.

[14] Sara Usama Jasim and Raaid Nawfee Hassan. Investigation of numerical simulation for adaptive optics system. *Iraqi Journal of Physics*, 21(3):9–23, 2023. Published: September 1, 2023.

[15] Mahmood K. Mirdan, Raaid N. Hassan, and Bushra Q. Al-Aboodi. Modeling and comparison of closed-loop and open-loop adaptive optics systems. *European Scholar Journal*, 3(5):–, May 2022. Published: 10 May 2022.

[16] Bertin Alpao. Deformable mirrors. https://www.alpao.com/products-and-services/deformable-mirrors/, 2026. Official product page.

[17] Xiao-xia Yang, Yu-mei Yin, and Xian-jun Wang. Numerical simulations for adaptive optics system. In *Proceedings of the 31st Chinese Control Conference*, Hefei, China, July 2012.

[18] Cédric T. Héritier, Christophe Vérinaud, and Carlos Correia. Oopao: Object oriented python adaptive optics. *Proc. SPIE*, 2021.

[19] François Leroux, Mojtaba Taheri, Idir Boudjema, Bruno Martin, Armin Schimpf, Anne-Sophie Bruni-Favier, Pierre Jouve, Eric Stadler, Paul Rouquette, Camilo Weinberger, Jérôme Schmidt, Benoit Neichel, Romain Fetick, and Thierry Fusco. Papyrus: Design and integration of the shack-hartmann branch. In *Adaptive Optics for Extremely Large Telescopes VII*, Avignon, France, June 2023. ONERA.

[20] Romain Fetick, Thierry Fusco, Arnaud Striffling, Eduard Muslimov, Jean-François Sauvage, Cédric Taïssir Héritier, Jonathan Dray, Sylvain Cetre, Vincent Chambouleyron, Idir Boudjema, Edoardo Bellone, Mahawa Cisse, Colin Dartevelle, Alexis Carlotti, Benoit Neichel, Bruno Martin, Jérôme Schmitt, François Huppert, François Dolon, and Marc Ferrari. Papyrus: From an adaptive optics system to an instrumental platform. In *SPIE Astronomical Telescopes + Instrumentation*, page 1309716, Yokohama, Japan, June 2024. SPIE.

[21] Szymon Gladysz, Julian C. Christou, L. William Bradford, and Lewis C. Jr. Roberts. Temporal variability and statistics of the strehl ratio in adaptive-optics images. *Publications of the Astronomical Society of the Pacific*, 120:1132–1143, October 2008.